Measuring the Transmission Matrix of Single Polystyrene Spheres

Roman Danser B.Sc.

Utrecht University
Faculty of Science

Debye Institute for Nanomaterials Science

Nanophotonics Research Group

Supervised by
Prof. dr. Allard Mosk
Prof. dr. Sanli Faez
Daily supervisors
dr. Itir Bakis Dogru Yuksel
Freya Whiteford
January 31, 2023

Abstract

Photonic crystals with a bandgap in the visible spectrum are needed for faster computing in the future, because of their light manipulation application. The packing arrangement of atoms in quasicrystals has opened a new area of materials that can have their band gap in this desired frequency range. In this research we look into the scattering behaviour of single crystals using a transmission matrix (TM) measuring experimental setup. These TMs, together with the amplitude and phase plots of these crystals, have shown that the setup is able to analyse single particles of 10 μm in diameter.

Contents

Introduction

Light is a spectacular phenomenon which allows us to see the world around us. During day-time, when solar radiation reaches our side of the earth, the electromagnetic radiation from the sun interacts with everything it touches. It can get absorbed, reflected back or even being scattered in all different directions [1]. Although only a small part of the electromagnetic spectrum can be perceived by the human eye, it is this small part that makes the world around us look so colourful [2]. The leaves of trees and plants, for example, contain little chloroplasts that absorb most of the frequencies that fall inside the visible part of the electromagnetic spectrum. However, we see the leaves as green, because the specific wavelength of the colour green, which is $\sim 510\ nm$, is not being absorbed by the chloroplasts, but reflected back [3].

Besides giving us the ability to see the world around us, light has given us much more than just colours and contrast. Less energetic frequencies for example, which is radiation with longer wavelengths, are radio waves ($\sim 10^3\ m$) that transmit information so that you can listen to music in your car [4]. Or infrared waves ($\sim 10\ \mu m$) that are not visible to the human eye, but can be detected using thermal cameras. Higher frequencies like ultraviolet or X-ray also have some very useful applications. UV-light is being used to purify drinking water from any organic micro pollutants [5], whereas X-rays are widely being used in medical imaging or airport security.

For all these applications, our control over both the radiation we produce and how we detect or capture the information it contains, is key. This is why there is an ever growing field of finding new and more efficient ways of controlling the light we use to transfer data and information. The computers used nowadays transfer and store information using electrons, but if this could be switched to photons, it would enable us to move to both higher bandwidths and faster data processing. A photon is a quantum of the electromagnetic field and moves at the speed of light, the frequency with which a photon travels is completely dependent on the energy it is given [6]. This is a parameter we can control, however, controlling and manipulating the travelling light is something completely different.

Photonic crystals are materials that have the ability to manipulate light

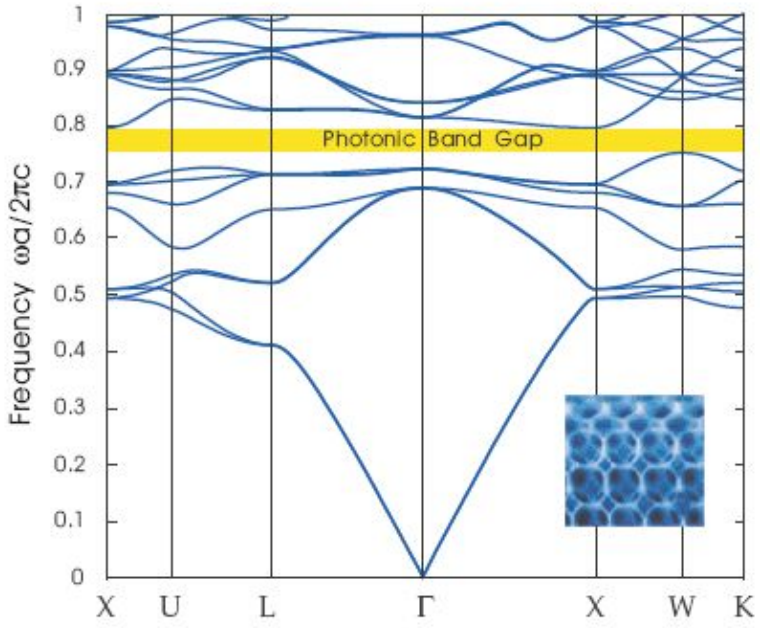

Figure 1.1: Photonic band diagram of a closed packed face centered cubic (fcc) arrangement of spheres [7].

in whatever way you want, this is because they contain a band gap. This is an energy range where no electronic states can exist, an example is the yellow band in Fig. 1.1. Inside this band gap, there is a range of frequencies that are completely blocked by the crystal, because of destructive interference of these frequencies inside the crystal [8, 9]. By introducing defects one can manipulate this band gap, after which for example the flow of light can be channeled extremely precise. Creating these photonic crystals has been done in all 3 dimensions so far. A 1D photonic crystal, a flat surface, can act as an extremely high reflectivity mirror for specific wavelengths. Photonic crystal fibers, 2D rods, are used for fiber optic communication. But the 3D photonic crystals, which of course have the most applications, are also the hardest one to make. Controlling the range of frequencies of their band gap is the difficult point, but 3D photonic crystals with a band gap in the infrared part of the spectrum have been synthesised and are already being used in the future generation of faster computing and information technology.

But, although this is already a big improvement on our speed of data

transferring, being able to use a broader bandwidth would be more ideal and open up more possible applications. Where crystals are defined by specific packing and arrangement laws of their atoms, it is this exact arrangement order of atoms that determines what frequencies fall into the band gap of the crystal. Minor changes or alterations in the arrangement of the atoms will lead to two different things: Firstly, the newly created material isn't considered to be a crystal anymore but rather a quasicrystal. Secondly, these quasicrystals have the possibility that their range of band gap frequencies falls into the visible light spectrum [10].

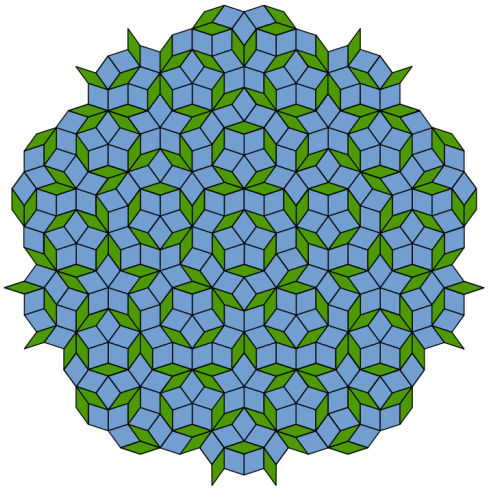

Figure 1.2: Quasiperiodic Penrose tiling.

Quasicrystals differ from crystals because their unit cell cannot be periodically repeated forever in the lattice configuration. They were discovered in 1984 by Daniel Shechtman for which he received the Nobel Prize in Chemistry in 2011 [11]. Their atomic structure is ordered, just like in crystals, but because it is not periodic, the most beautiful lattice configurations can arise. An example of such an aperiodic tiling is the Penrose tiling, see Fig. 1.2. Their aperiodic tiling is also visible in the diffraction pattern of quasicrystals. The diffraction pattern of a crystal always has rotational symmetry, but it can only be two-, three-, four- or six-folded [12]. However for quasicrystals, five- and even ten-fold rotational symmetry have been observed in their diffraction patterns [13–15]. This is another indication that these structures lack translational symmetry, although their atoms are ordered and fill up all available

space as tightly packed as possible. A recent discovery by the Soft Condensed Matter group at the Utrecht University showed a self-assembly route of mixtures of binary nanoparticles leads to a 3D icosahedral quasicrystal with a diameter of $\sim 170\ nm$ [16].

These newly formed materials need to be analysed and optimised to find the optimal packing arrangement of atoms that has the desired band gap frequency range. Their approximated spherical shaped band edges differ from their 1D and 2D slab- or cube geometry lower dimension quasicrystal band edges, and thus need to be analysed differently. To find their scattering eigenstates, an instrument that can measure both amplitude and phase of scattered waves of these spherical quasicrystals is needed. In this thesis a start is made towards creating and characterising such an instrument. The setup has already been used to observe scattering invariant modes and improve imaging inside highly scattering materials [17]. Here, we use small polystyrene crystal spheres, similar in size to the desired 3D quasicrystal, to find out whether this setup is compatible with small spherical particles instead of flat materials.

Theory

In order to extract information from both the amplitude and phase of scattered waves from our spherical polystyrene particles, we need to understand the basics of light scattering. Then we can identify the scattering regime, relevant for our particle scattering, which we can use to optimise our analysis technique, which is measuring the transmission matrix (TM). Optical TMs are the mathematical representation of the transmission operator (TO) of the sample, which relates any incident field to the transmitted field. Finally, an introduction to Mie scattering theory is given, which is used to calculated simulated TMs of our spherical polystyrene particles.

2.1 Light scattering

As light passes through an object, it is scattered by the particles inside this medium, which are called microscopic scatterers. When no absorption takes place during the scattering event, the light waves' energy is conserved. An example of this is the colour of milk being white; none of the visible wavelengths are absorbed, which means the reflected and scattered light that reaches our eyes contain all the colours of the rainbow. The sun however, is not white, this is because our atmosphere is full of small particles that mostly scatter the blue wavelengths of the sun light. Hence, the sky looks blue and the sun yellow.

As light passes through these small particles, the size of these particles determines the number of scattering events of the light that take place inside them. The smaller the particle, the faster the light exits on the other side, thus less scattering events could have taken place. Besides, the wavelength of the light passing through a particle is also of great importance. These two parameters are expressed as the size parameter:

$$x = 2\pi r/\lambda, \tag{1}$$

where r is the radius of the particle, and λ is the wavelength of the light passing through the particle. Three different regimes for the scattering of light by spherical particles are considered using this size parameter.

We speak of the Rayleigh scattering regime when x << 1, in this regime the particles are much smaller than the radiation wavelength [18]. For x $\sim$ 1, the wavelength of the radiation and the particle size are comparable. This is considered to be the Mie scattering regime [19, 20]. Finally, when the scattering sphere is much larger than the wavelength (x >> 1), the geometrical optics regime should be considered. Here, the incident radiation is described as a wavefront containing many individual light rays that can interact individually with the scattering medium.

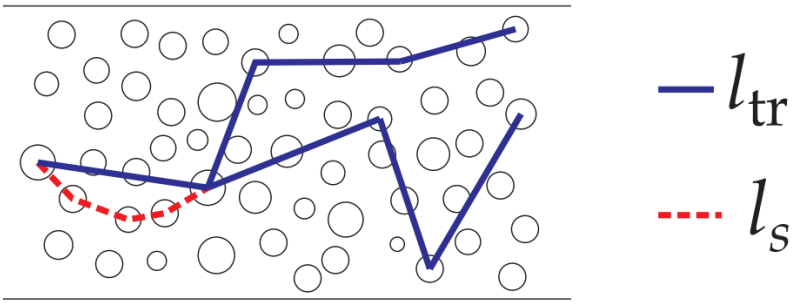

Figure 2.1: Schematic representation of both scattering and transport mean free path for anisotropic scattering [21].

A schematic representation of a single light ray interacting with an anisotropic scattering medium is given in Fig. 2.1. The individual particles in this medium interact with the light ray by scattering the initial direction of the ray into a different direction. The distance between such scattering events is called the scattering mean free path (l_s), after which scattering occurs. If this scattering is mostly in the forward direction, the medium is considered to be anisotropic. But if scattering can happen in any random direction, the medium is considered to be isotropic. Multiple anisotropic scattering events eventually lead to a randomised propagation path of the incident light ray inside the medium. This distance is called the transport mean free path:

$$l_{tr} = \frac{l_s}{1 - \langle cos\theta \rangle}. \tag{2}$$

Here, $\langle cos\theta \rangle$ indicates that we average over all angles θ, which is the angle between the vector of the incident ray and the vector of the scattered ray. For an isotropic scattering event $\langle cos\theta \rangle = 0$, meaning the light is randomised.

Whereas for $\langle cos\theta \rangle = 1$, the direction of the scattered light is completely in the forward direction, so it is never randomised.

In many anisotropic materials, such as zinc oxide, the following inequality holds:

$$\lambda < l_s \leq l_{tr} << L << L_{abs}, \tag{3}$$

where L is the distance from one side of the material to the other side of the material and L_{abs} is the absorption length. In this regime, the diffusive regime [22], the light rays scatter through the medium in a random walk, causing a plane wave to be scattered into many different directions, which creates a speckle pattern on the detector, see Fig. 2.2 (a).

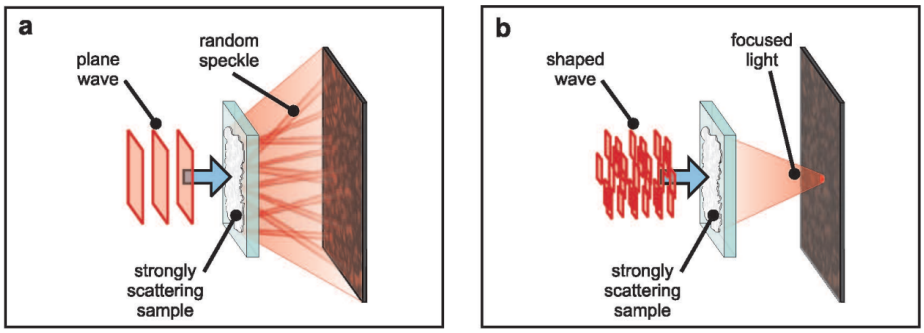

Figure 2.2: Concept of wavefront shaping. (a) A plane wave is scattered by a disordered medium into a speckle pattern in the detection plane. (b) A shaped wavefront is focused by the disordered medium onto a targeted area in the detection plane [23].

A stable, non-vibrating strong scattering sample, such as a piece of white paint, has the same speckle pattern if the same plane wave is projected onto the same incident spot. This indicates that each scatterer scatters the light rays exactly the same over time. Thus, knowing the position of these scatterers and their scattering behaviour, one could manipulate the incoming wave such that it is scattered into one single speckle on your detector, as depicted in Fig. 2.2 (b). This is the concept of wavefront shaping; the phase and amplitudes of individual rays of a beam of light are optimised in such a way that all of the light projected onto a strongly scattering medium is focused into one spot [23].

The wavefront shaping technique works really well, the only downside is that, upon moving the scattering material, all the information of the scatterers

is completely lost. Since the incoming light comes in at different angles and interacts with different scatterers, one has to re-optimise the wavefront to find the optimal phase and amplitude of each individual light ray. This does however also show that the scattering behaviour information of these scatterers can be stored. In fact, if we want to know exactly how a medium would interact with an incoming wavefront, the scattered, or rather transmitted field, can be calculated using the transmission operator (TO) of this medium. Because the TO links any incident field to its corresponding transmitted field. Experimentally resolving this TO is nearly impossible though, because some scattered or transmitted waves will always fall outside the apertures of your apparatus. However, the TO can be approximated by the transmission matrix (TM), which is a mathematical representation of the TO [24, 25].

2.2 Transmission matrix

Where the TO of a scattering medium links any incident field to its corresponding transmitted field, the TM is a representation of a small part of this TO, defined by the number of incident and transmitted modes that are chosen beforehand. This gives us two identical grids, one that contains all the incident modes, and one that contains all the transmitted modes. With the scattering medium being in between these two grids, which are N modes big. If a single incident mode is projected onto the medium, a speckle pattern is created on the transmitted grid, with some modes detecting light, and some modes detecting no light at all. Doing so for each incident mode, one would end up with an NxN matrix that shows the relation of each incident mode to all the transmitted modes. Since scattering can change the polarisation of light, this has to be taken into account in a TM. By defining two orthogonal polarisations of light, which we call horizontal and vertical, a polarisation complete 2Nx2N TM can be measured, containing four sub-matrices (T_{HH}, T_{VV}, T_{HV} & T_{VH}). Each of these sub-matrices represents both one of the two incident polarisation components and one of the two transmitted polarisation components. The T_{HV} sub-matrix for example, links the incident horizontal polarised field to the transmitted vertical polarised field.

A simulation example for a non-scattering sample, like glass or air, is given in Fig. 2.3 (a). Both the incident and transmitted grids are made out of 919 individual modes. The value of each of the diagonal elements (Fig. 2.3

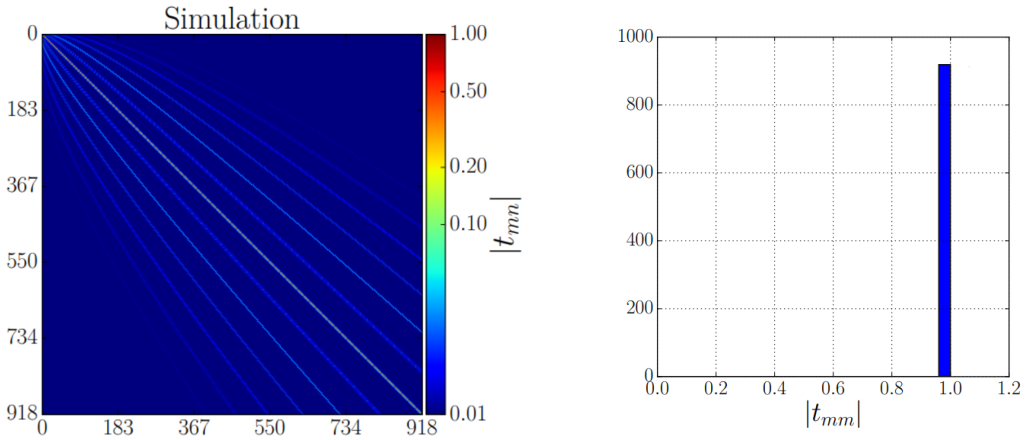

(a) (b)

Figure 2.3: (a) Simulated 919x919 TM elements for the T_{HH} polarization components of glass. (b) Histogram of magnitude of diagonal elements. Figure taken from [26].

(b)) is one, indicating that there was no scattering behaviour for any of the incident modes as it passed through the glass sample. This should have given a complete dark matrix with one intense diagonal, the simulation however shows side diagonals. These side diagonals are caused by the field overlap integral of one mode on the detection grid with its neighbouring modes.

This overlap is caused by the Airy disk produced by a collimated beam in the focal plane, see Fig. 2.4. This Airy disk is formed when a circular laser beam, with a uniform intensity across the circle, is focused by a lens. A more intense beam in the focus point will create a bigger Airy disk. As depicted in Fig. 2.4, the central intense Airy unit is surrounded by less intense concentric rings that alternate with local intensity minima. These rings are produced by Fraunhofer diffraction of light by circular apertures [28]. This causes overlap

Figure 2.4: Three-dimensional rendering of an Airy disk [27].

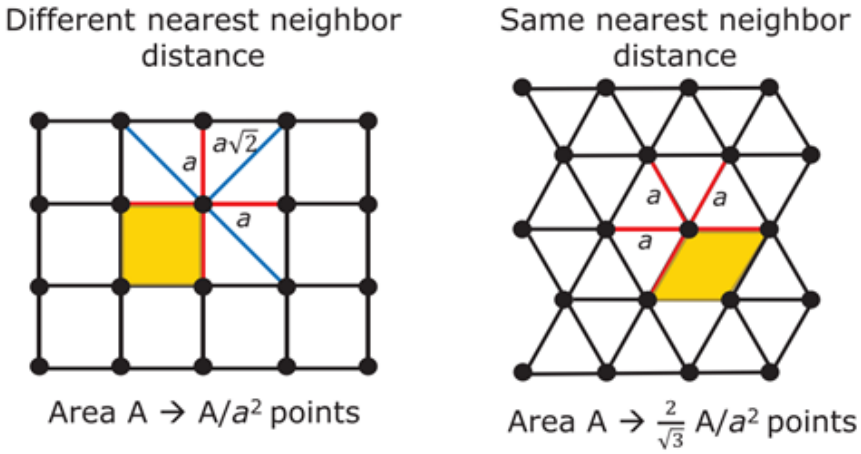

Figure 2.5: Two sampling lattice grids with lattice constant a, with the yellow parts representing a unit cell. The left grid is a square lattice and the right grid an hexagonal lattice [26].

between the individual modes in the detection grid when they are sampled too close together. The modes need to be close-packed to extract the most information out of our scattering medium. However, this close-packing means these concentric rings with alternating local minima and maxima end up on neighbouring modes, resulting in a measured field overlap integral. These overlap integrals show up as the side diagonals in our TMs of non-scattering media.

To minimise these noise effects, the sampling configuration of the two grids has to be chosen in such a way the overlap integral between neighbouring modes is, firstly, minimal, but secondly, also constant. A triangular lattice, or hexagonal lattice, is the optimal sampling configuration to achieve this. The right image in Fig. 2.5 shows that all the six nearest neighbours are at a distance a, which is the lattice constant, while the six next nearest neighbours are at a distance $a\sqrt{3}$. In a square grid, shown on the left image in Fig. 2.5, there are eight nearest neighbours who are at different lattice constant a distances from the central mode. Four neighbours are at a distance a, with the other four being at a distance $a\sqrt{2}$. It is this separation distance difference between two spots that yields different overlap integrals, thus the optimal lattice constant a at critical sampling has to be determined before creating

our incident field grid.

Critical sampling for the square lattice is achieved at:

$$a_{sq}^2 = \frac{\lambda^2}{\pi}(NA)^{-2}, \tag{4}$$

and for the hexagonal lattice this is achieved at:

$$a_{hex}^2 = \frac{2}{\sqrt{3}}\frac{\lambda^2}{\pi}(NA)^{-2} \approx 1.15\frac{\lambda^2}{\pi}(NA)^{-2}, \tag{5}$$

where NA is the numerical aperture. From these equations we learn that critical sampling depends on both the wavelength of the light and the numerical aperture used in our experimental setup. Interestingly, near the critical sampling on the hexagonal grid, the nearest neighbour Airy spots are almost exactly at the Rayleigh criterion:

$$a_{hex} = 0.994 a_{Ray} \quad \text{with} \quad a_{Ray} = \frac{z_1\lambda}{2\pi}(NA)^{-1}, \tag{6}$$

with a_{Ray} being the Rayleigh distance [29]. Here, the maximum of the neighbouring Airy spot overlaps with the first zero of the central Airy spot, causing the field overlap integral to disappear. Also, $z_1 \approx 3.83$, which is the first zero of the J_1 Bessel function [30]. Using this, the nearest neighbours at critical sampling have almost zero overlap, with the overlap of the next nearest neighbours also being low. Besides this useful feature of the hexagonal grid, the unit cell of this grid, see yellow part in Fig. 2.5, is also smaller than the unit cell of the square lattice. This gives the hexagonal grid around a 15% higher sampling density, allowing TM scans to cover larger fractions of the complete TM. Thus representing the scattering properties of our medium more faithful than if the square grid were to be used.

This can be checked by plotting a histogram of the singular value distribution of a non-scattering sample. The singular values of a TM correspond to the transmission eigenchannels of the sample, if the TM accurately represents the TO [31].

It was shown by Pai et al. that there is a clear difference in the singular value distribution for the hexagonal grid sampling or the square grid sampling [32]. They proved that the singular values of glass, in the polarisation submatrices, normalised to the root mean square (RMS) singular value of the

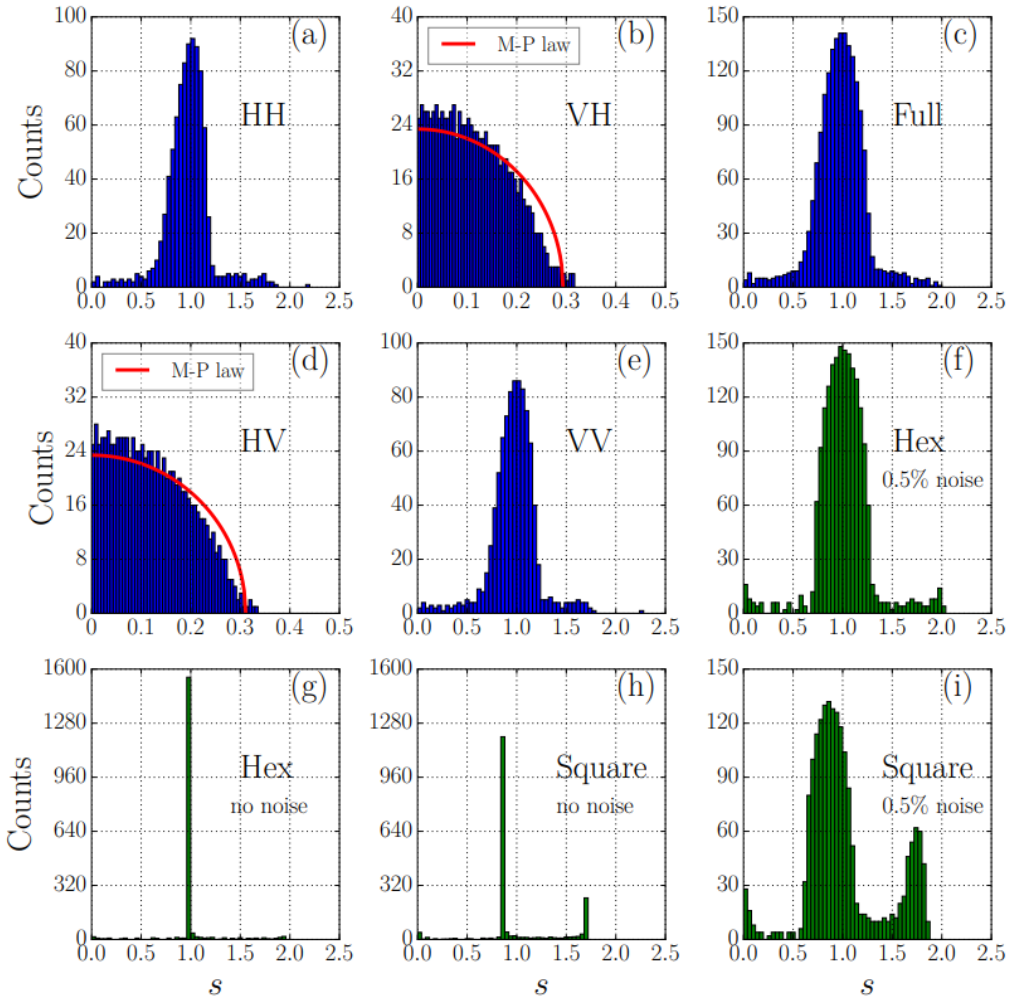

Figure 2.6: (a,b,d,e) Singular value histograms of sub-matrices of a measured TM of glass and (c) of a polarization complete TM. (f) Simulated histogram of singular values of complete TM with hexagonal grid sampling with 0.5% RMS noise and (g) without noise. (i) Simulated histogram of singular values of complete TM with squared grid sampling with 0.5% RMS noise and (h) without. Red line in (b) & (d) corresponds to Marchenko-Pastur law. Figure taken from [26].

respective co-polarised sub-matrix, cluster around 1.0 for both the T_{HH} & T_{VV}

polarisation sub-matrices (Fig. 2.6 (a)&(e)) and follow the Marchenko-Pastur law in both the T_{HV} & T_{VH} cross-polarisation sub-matrices (Fig. 2.6 (b)&(d)). Since glass does not scatter the light that is projected orthogonally onto its surface, the transmission eigenchannels in both polarisation sub-matrices T_{HH} & T_{VV} should be completely transmittent. The singular values of these sub-matrices cluster around 1.0, just like for the singular values of a full polarisation complete TM (Fig. 2.6 (c)). Taking into account a minimal amount of noise, it can be concluded that the transmission eigenchannels indeed transmit 100% of the light that is projected onto them. On the other hand, the singular value distribution of the cross-polarisation sub-matrices tells us these are random uncorrelated matrices; their singular value distribution is in line with the Marchenko-Pastur law, which predicts the singular value probability of a random uncorrelated matrix [33].

With the measured TM of a scattering medium, one can locate its transmission eigenchannels, if there are any, and find out their transmittance. An example is shown in Fig. 2.7, in which light is coupled to all the 2282 individual transmission eigenchannels of a 2.7 µm scattering sample [34]. For all channels the reflectance $\tilde{R}^{(n)}$ and transmission $\tilde{T}^{(n)}$ add up to 1, meaning

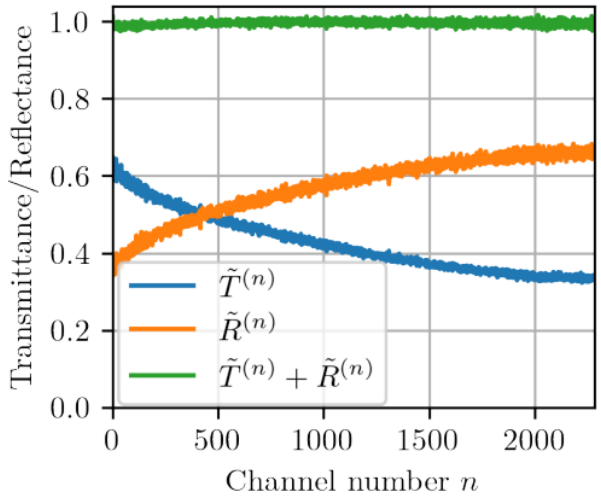

Figure 2.7: Reflectance $\tilde{R}^{(n)}$ and transmittance $\tilde{T}^{(n)}$ versus channel number for a 2.7 µm sample with average transmittance $\tilde{T}_{avg} = 0.45$. Figure taken from [34].

the used setup captures the same fraction of light in both transmission and reflection for each individual channel. The maximum measured transmittance $\tilde{T}^{(n)}$ is almost 0.65. Coupling light to these channels would thus enhance the overall transmitted light by this random scattering sample than by just illuminating it with a plane wave, because on average, the transmittance $\tilde{T}_{avg}$ = 0.45.

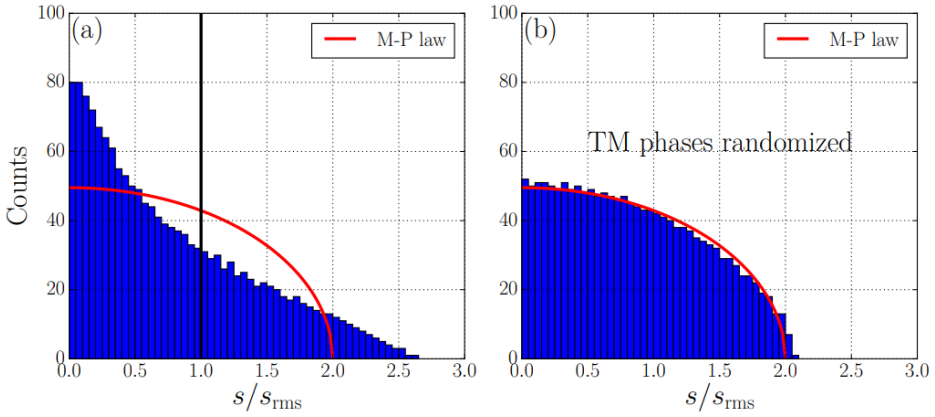

Figure 2.8: Singular value distribution of TM normalized to RMS value, of a random scattering material (a) and for a TM with all the elements being randomised (b). Red line corresponds to Marchenko-Pastur law. Figure taken from [26].

Using the polarisation complete TM of the same random scattering material, a singular value distribution normalised to the RMS value can be plotted, Fig. 2.8 (a). Unlike for the non-scattering medium, the values are not clustered around 1. Also, they are not random, since a TM with random elements would follow the Marchenko-Pastur curve, just like in Fig. 2.8 (b), but the experimental data shows a tail of singular values that have a high transmittance. A start into deriving a theoretical way of predicting the transmittance of these individual eigenchannels using free probability theory has been made [35]. Here, the theoretical distribution coincides really well with the lower transmitting eigenchannels distribution, but it is still unable to predict the distribution of the higher transmitting eigenchannels.

2.3 Mie scattering theory

The TM has proven to be a strong tool to control the scattering of light in diffusive media. It can locate highly transmitting transmission eigenchannels, thereby overcoming the randomness in big random scattering materials. However, in this thesis we are interested in smaller, non-random, single spherical particles. The scattering of light by such particles can be explained using Mie scattering theory, which will be used to simulate TMs of our desired single polystyrene spherical particles.

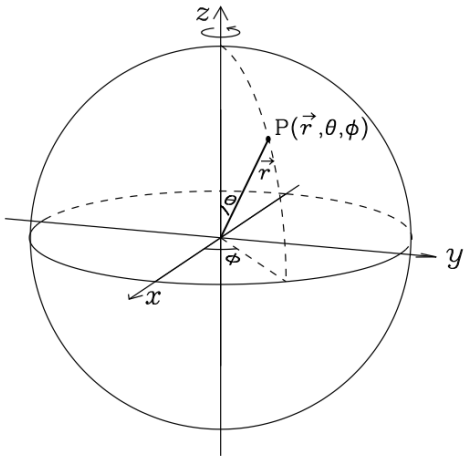

Figure 2.9: Spherical polar coordinate system, figure taken from [36].

Mie theory is the solution to the scattering of an electromagnetic plane wave by a single homogeneous sphere, named after its developer Gustav Mie [37]. A physically realisable time-harmonic electro-magentic field (**E**, **H**) in a linear, isotropic, homogenous medium, must satisfy the wave equation [20]. Besides, **E** & **H** are not independent of each other. To construct a solution to the wave equation as a vector function **M**, an arbitrary constant vector c and a scalar function ψ are given such that:

$$\mathbf{M} = \nabla \times (c\psi), \tag{7}$$

where ∇ is the nabla operator, which here denotes the divergence of the vector field in three-dimensional Cartesian coordinates. Since we are interested in a sphere, the scalar function ψ is chosen in such a way it satisfies the wave equation in spherical polar coordinates r, θ & ϕ, visualised in Fig. 2.9. Changing the arbitrary vector c to the radius vector **r** results in:

$$\mathbf{M} = \nabla \times (\mathbf{r}\psi). \tag{8}$$

Now **M** is also a solution to the wave equation in spherical polar coordinates,

with the scalar wave equation in spherical polar coordinates being:

$$\frac{1}{r^2}\frac{\partial}{\partial r}(r^2\frac{\partial\psi}{\partial r}) + \frac{1}{r^2 sin\theta}\frac{\partial}{\partial\theta}(sin\theta\frac{\partial\psi}{\partial\theta}) + \frac{1}{r^2 sin\theta}\frac{\partial^2\psi}{\partial\phi^2} + k^2\psi = 0, \tag{9}$$

which is used to determine the boundary conditions of our system, where k is the wave vector: $k^2 = \omega^2\epsilon\mu$, with ω being the frequency, ϵ the complex permittivity and μ the permeability

A straightforward way to determine the relation between an incident field with its transmitted field through an object, is by multiplying it with the amplitude scattering matrix and the wave function:

$$\begin{pmatrix} E_{\parallel_s} \\ E_{\perp_s} \end{pmatrix} = \frac{e^{ik(r-z)}}{-ikr}\begin{pmatrix} S_1 & S_3 \\ S_4 & S_2 \end{pmatrix}\begin{pmatrix} E_{\parallel_i} \\ E_{\perp_i} \end{pmatrix}, \tag{10}$$

with $E_{\parallel_i}$ & $E_{\perp_i}$ being the two polarisations of the incident field and $E_{\parallel_s}$ & $E_{\perp_s}$ the two differently polarised scattered fields. The elements S_1, S_2, S_3 & S_4 of the amplitude scattering matrix depend on both the scattering angle θ and the azimuthal angle ϕ. For spherical particles, the series expansion of the scattered field is uniformly convergent, and can therefore be stopped after a sufficient number of n_c terms without the resulting error becoming too large. The S_3 & S_4 elements are zero for scattering by spherical particles, with the other elements S_1 & S_2 being:

$$S_1 = \sum_n \frac{2n+1}{n(n+1)}(a_n\pi_n + b_n\tau_n), \tag{11}$$

$$S_2 = \sum_n \frac{2n+1}{n(n+1)}(a_n\tau_n + b_n\pi_n), \tag{12}$$

where a_n & b_n are the external field coefficients, depending on the size parameter x, calculated by Eq. (1), and complex refractive index m of the particle [38]. Whereas π_n & τ_n are angle-dependent functions:

$$\pi_n = \frac{P_n^1}{sin\theta}, \qquad \tau_n = \frac{dP_n^1}{d\theta}, \tag{13}$$

where P_n denotes the Legendre polynomials. π_n & τ_n can be computed by upward recurrence from these relations:

$$\pi_n = \frac{2n-1}{n-1}\mu\pi_{n-1} - \frac{n}{n-1}\pi_{n-2}, \tag{14}$$

$$\tau_n = n\mu\pi_n - (n+1)\pi_{n-1}, \tag{15}$$

here $\mu = cos\theta$.

Using Eq. (10), for any incident field defined as an incoming vector focused on a spherical particle, all the scattered vectors with their according field intensities can be calculated. These intensity values are ratios compared to the total incident field intensity, with most of the light not being scattered and propagating in the forward direction ($\theta = 0^o$), giving this single propagating vector the highest ratio value, visualised in Fig. 2.10. Since we know the ratio of each scattered vector right after it is scattered by the particle using the simulation, the far field wave function can be neglected and the scattered and detection plane can be placed in the same field.

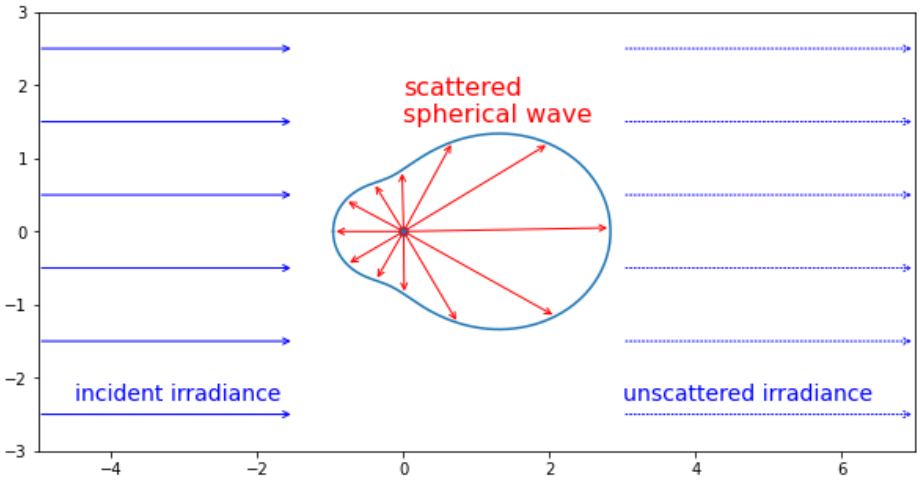

Figure 2.10: Schematic of scattering of a spherical wave by a single spherical particle.

By supplying the simulation code with the complex refractive index of polystyrene and the diameter of our particle, the PyMieScatt library[1] calculates the S_1 & S_2 elements. By defining our hexagonal incident, and subsequent detection grid, the ratio for each scattered vector is calculated, for both polarisations of light. The results of these simulations are presented and analysed in section 4.1.

[1]An open-source module for Python that contains functionality for solving the inverse problem for complex m using extensive optical and physical properties as input, and calculating regions where valid solutions may exist within the error bounds of laboratory measurements [39].

Experimental setup

The optical TMs are experimentally measured using a complex experimental setup that has been build by dr. Jeroen Bosch [34]. Here, the setup is split into three sub modules to describe all its functionalities. First the incident fields are created, which are then focused onto the sample to create the transmitted fields. Finally, these fields are detected using off-axis holography after which the TM of our sample can be reconstructed.

3.1 Wavefront construction module

In the first part of the setup, the random light fields, that are projected onto the sample, are created. These fields consist of many pixels, or individual light rays, of which both the phase and amplitude are controlled. Besides, to get the polarisation complete TM of our medium, the phase and amplitude of the two different polarisations need to be modulated. For this, a digital micromirror device (DMD) with a resolution of 1920x1200 mirrors, is used. As depicted in Fig. 3.1, the light beam is widened to a beam with a diameter of 18 mm using a fiber collimator (C1). Next, it is split into two orthogonal

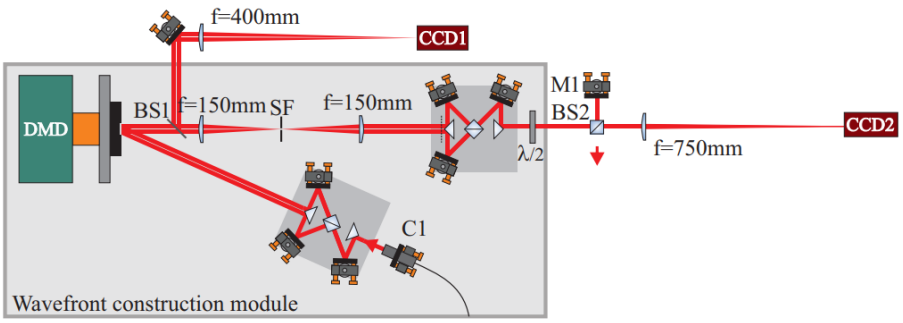

Figure 3.1: Field synthesis module, figure taken from [34].

parallel orthogonal polarisation components by a polarising beam splitter (PBS), which are reflected of two different regions on the DMD. Each DMD

region generates a circular light field with a diameter of 636 mirrors of which both the local phases and amplitudes are controlled. After reflection, the fields are Fourier filtered using a 4f-configuration and an aperture to enhance the accuracy of the modulated light field. Using the same configuration as for the splitting of a single beam, the two orthogonal polarisation components are recombined. The two configurations that split and recombine the two polarisations of light are mounted at an angle of 45^o, which gives a beam with two diagonal polarisation components. A half-wave plate ($\lambda/2$) rotates these two components such that the beam contains both a horizontal and a vertical polarisation component.

3.2 Imaging module

The generated fields are projected onto the sample in the imaging module, which is shown in Fig. 3.2. Here, the incident and transmitted fields are focused and collected by two high numerical aperture objectives. These are capable of collecting a large fraction of the power while achieving a high spatial resolution. The fields are projected onto the sample using the 0.95NA, 63x objective, and collected by the 1.4NA, 63x oil immersion objective. Using these magnifications, each individual mode field, that all combined make up the complete hexagonal incident field, is mapped to a spot with the size of the diffraction limit on the surface of the sample:

$$\delta = \frac{\lambda}{2NA}. \tag{16}$$

Fig. 3.2 shows both diffraction limited spot sizes as well as the maximum incident and transmitted angles for the two numerical aperture objectives. These objectives are mounted on piezo stages that move with the direction of propagating the light beam. The glass cover slide, on which the sample is deposited, is mounted on a SmarAct stage that moves in the two orthogonal directions with respect to the propagation distance of the light beam. This gives full control over the control area and field of view, which has a radius of 23 μm.

To focus on the sample, temporally and spatially incoherent light is generated by the DMD by creating 160 different random phase patterns, which are projected sequentially onto the sample at 2000 fields per second.

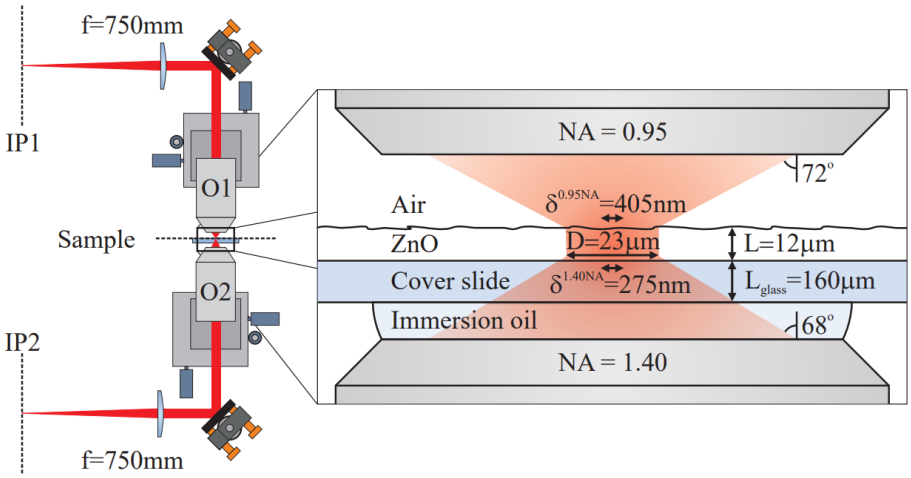

Figure 3.2: Imaging module, figure taken from [34].

By integrating over these patterns on the camera (the exposure time is set to 160/2000 = 0.08 seconds), the focal distances of both objectives can be found with an estimated accuracy of 1 μm. This focusing procedure works fine for big flat media that fill the complete field of view, like the ZnO layer depicted in Fig. 3.2. For the small spherical polystyrene particles, the objectives should be focused onto the surface of the sphere for the incident fields to pass through the complete particle, like depicted in Fig. 3.3. The smallness of these particles causes most of the light to just pass right next to it during the focusing procedure, which results in focusing onto the glass cover slide rather than on the single particle itself.

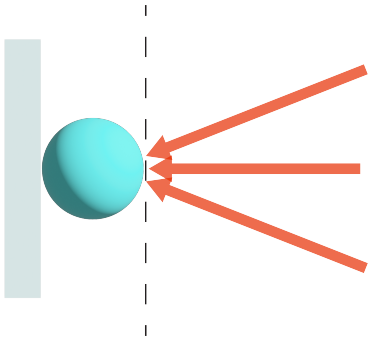

Figure 3.3: Ideal focal distance of objective where each incident field (red arrow) is focused onto the surface of a spherical particle (blue sphere), which is deposited on a glass cover slide (grey rectangle).

To prepare our glass cover slides with single polystyrene particles deposited onto its surface, a single droplet of a solution polystyrene particles

(Fluoresbrite^{TM} Carboxylate Microspheres from Polysciences, Inc.) was drop-casted onto the glass surface. These glass cover slides (170 μm thick) have been cleaned using a plasma cleaner, after which the droplet is left to evaporate over time. The polystyrene particles stick to the glass, mostly in small groups of two or three particles. After the water has evaporated, a single particle in the center of the field of view needs to be found, this is done by raster scanning the surface of the glass cover slide.

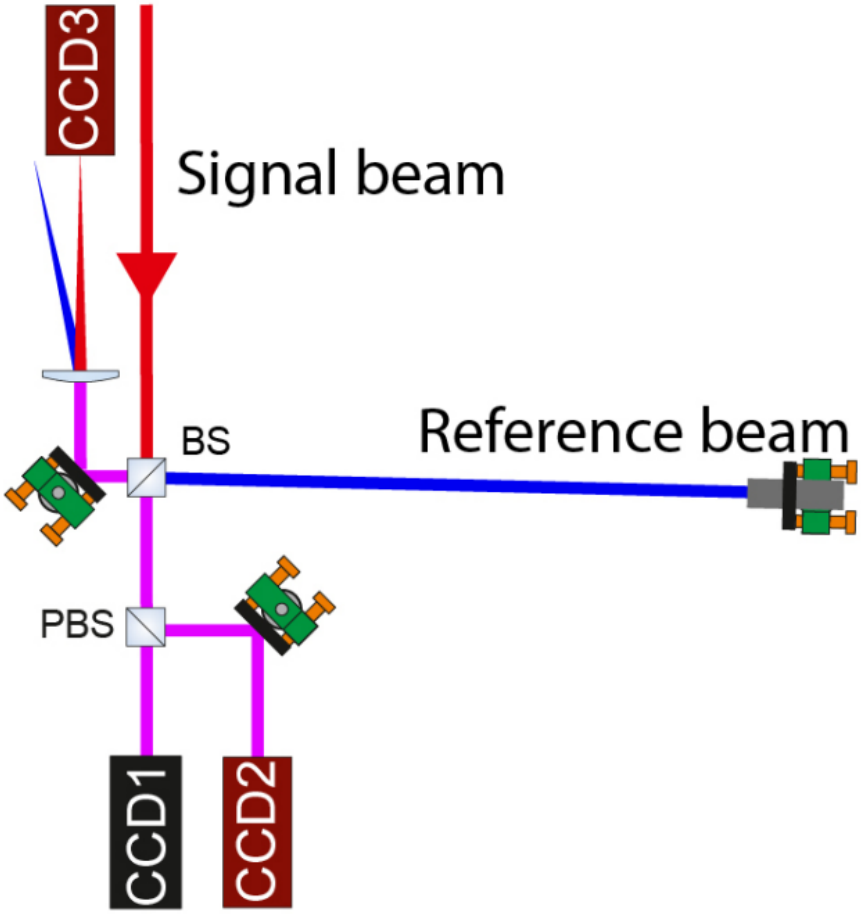

Figure 3.4: Field measurement module. Signal beam in red, reference beam in blue and overlapping beams in pink. Figure taken from [34]

3.3 Field measurement module

The transmitted fields contain a spatial field profile that we want to detect. For this, we analyse each polarisation separately, where we measure the local phase and amplitude of each field with off-axis holography [40].

The signal beam overlaps with a reference beam after a 50:50 beam splitter (BS), after which the light is split by a polarising beam splitter (PBS) into both the horizontal and vertical polarisation component, see Fig. 3.4.

By interference effects between the signal beam (E_s) with the slightly off-axis reference beam (E_0) on both CCD1 and CCD2 cameras, the complex image of the signal beam can be reconstructed. The interference of the two beams gives an intensity measured by the camera of:

$$I = |E_0|^2 + |E_s(x,y)|^2 + E_0 E_s^*(x,y)e^{iksin\theta x} + E_0^* E_s(x,y)e^{-iksin\theta x}. \quad (17)$$

These terms correspond to the signals centered around the three spatial frequency orders 0, +1 & -1: 0=($|E_0| + |E_s|$), $v = \frac{ksin(\theta)}{2\pi}$ and $-v$. If the spatial frequency v is larger than the maximal spatial frequency in the signal to reconstruct, the Fourier transform of the measured intensity pattern shows three individual components, the 0, +1 and -1 orders, which do not overlap. Here, the -1 order is directly proportional to the complex signal field E_s, shifted by the spatial frequency v. By centering around this order in the Fourier domain, the inverse Fourier transform gives the complex image E_s.

CCD3 measures the total transmitted intensity of the transmitted fields, because the reference beam does not fall on this camera due to the large angle it makes.

Results

In this chapter, the results of both simulations and experimental analysis are presented. It starts with the simulation data, and gives an explanation into how and why these results were obtained. Next, the experimental data and analysis results are shown. Again, in dept explanations and interpretations of the results and analyses are provided.

4.1 Simulation results

For the simulation of a polarisation complete TM of a single polystyrene sphere, the PyMieScatt library is used to calculate the S_1 & S_2 elements. Using these elements, the ratio of scattered light into each specific transmitted mode can be determined. For this, first the two vector fields of incoming

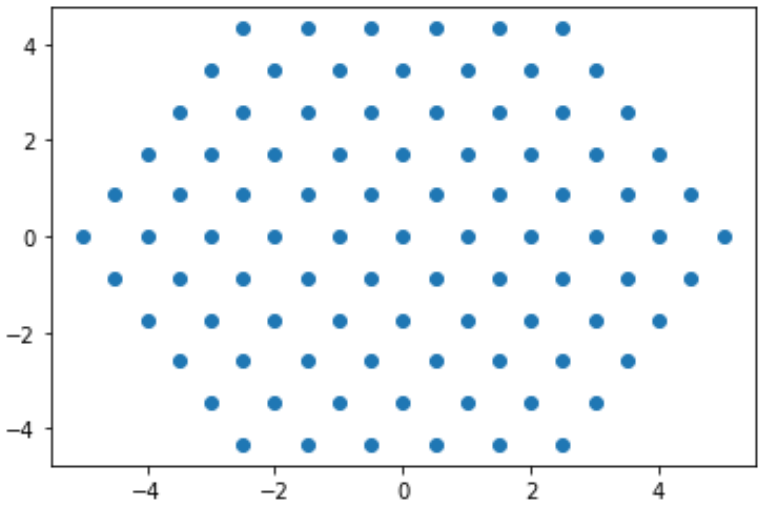

Figure 4.1: Hexagonal grid coordinates consisting of 91 individual modes, used for defining vector field of incoming and transmitted modes. Spacing between the modes is chosen such that the overlap integral between neighbouring modes is almost zero.

and transmitted modes are needed. However, since these two fields are the same, we can copy the incoming vector field to get the transmitted vector field. By making a hexagonal grid, as projected in Fig. 4.1, with the spacing between the modes set to such a value the overlap integral between the neighbouring modes is almost zero, all the incoming vectors onto the particle can be determined.

Using this vector field, the angles of the incoming and transmitted modes can be determined, which are some of the parameters used to calculate the S_1 & S_2 elements. The complex refractive index $m = n + ik$ of polystyrene can be calculated by:

$$n^2 - 1 = \frac{1.4435\lambda^2}{\lambda^2 - 0.020216}, \tag{18}$$

where λ is the wavelength of the light used in our experimental setup. Using this wavelength ($\lambda = 771\ nm$), m is set to $1.579 + 0$, because there is no absorption. Finally, the diameter of the particle is set to 1.58 μm, which results in a size parameter x of 6.438, calculated using Eq. (1).

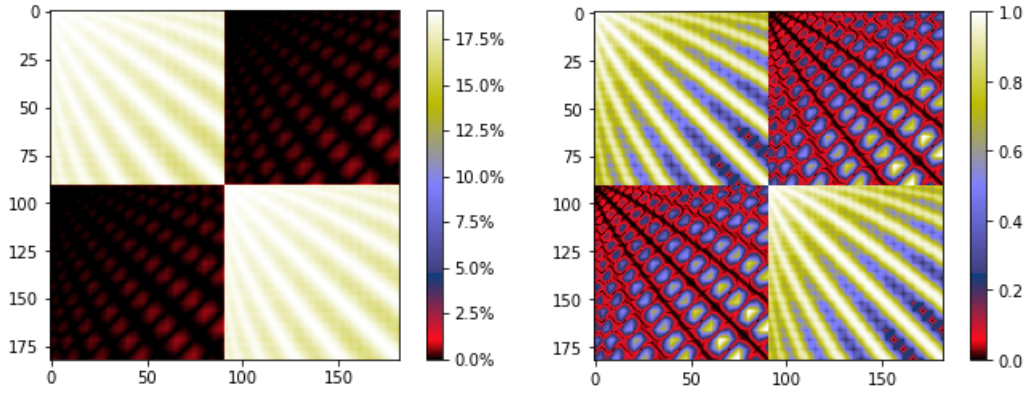

(a) (b)

Figure 4.2: (a) Simulated polarisation complete TM elements, measured with a hexagonal grid of 91 individual modes, of a single polystyrene sphere with diameter of 1.58 μm, and (b) its normalisation (each sub 91x91 matrix is normalised individually).

The resulting simulated TM is shown in Fig. 4.2 (a). Here, the four sub-matrices can clearly be distinguished, because these small particles barely

change the polarisation of the incident light. This makes the T_{HV} & T_{VH} cross-polarisation sub-matrices almost completely dark. The side diagonals, caused by overlap of a detected mode with some neighbouring modes are also visible in this result. However, this TM also tells us that these small spherical particles, with a diameter of 1.58 μm, barely scatter any light, since most of the light just propagates in the forward direction. This makes the central diagonal of the TM really intense, but also because of this, other details fade out.

To overcome this problem, which mainly happens in the cross-polarisation sub-matrices, each sub-matrix is normalised individually, which results in the TM in Fig. 4.2 (b). Normalising the complete TM would make the central diagonal even more bright than before. In the normalised TM, more details of our spherical particles light scattering behaviour can be extracted from the cross-polarisation sub-matrices. Although not perfectly spherical, many rectangular, or oval or a combination of these two, shapes can be made out. Combined with the black diagonal in these sub-matrices, we know that light propagating in the forward direction through a polystyrene sphere does not change its polarisation component. But when the light is scattered by the particle, a small portion of this scattered light changes its polarisation component.

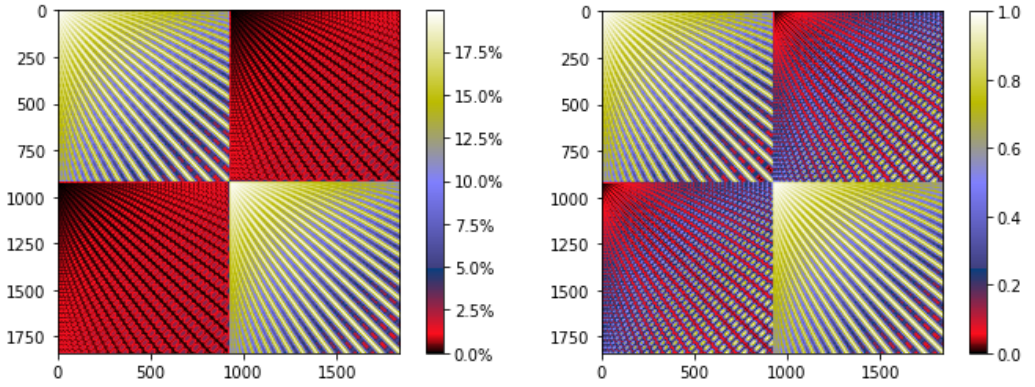

(a) (b)

Figure 4.3: (a) Simulated polarisation complete TM elements, measured with a hexagonal grid of 919 individual modes, of a single polystyrene sphere with diameter of 1.58 μm. (b) Normalised TM of (a) (each sub 919x919 matrix is normalised individually).

If the vector field is increased from 91 modes to 919 modes, besides the TM becoming much bigger, the biggest scattered modes show more polarisation shifts than the smaller scattered modes, as you see Fig. 4.3 (a). After normalisation of the individual sub-matrices (Fig. 4.3 (b)), the same rectangular/ oval shapes are present in the cross-polarisation sub-matrices. Based on these results we conclude that for particles this small (1.58 μm in diameter), measuring the TM with an incident field containing more than 91 incident modes does not result in more particle scattering information than if an incident field with 91 modes is used.

To be able to compare our simulation results with our experimental results more faithfully, two extra TM simulations were performed. For these simulations all the parameters were exactly the same as for the last simulations, with the incident grid containing 91 modes and increasing the polystyrene sphere size. These new particle diameters were 5 μm & 10 μm, experimental data of these polystyrene particle sizes will be shown in Fig. 4.2, simulation results are shown in Fig. 4.4.

The first noticeable difference with the previous simulations is the decrease in intensity of the central diagonal. This is to be expected, because our particles are bigger. The light has to travel a longer distance to get to the other side of the particle, thereby increasing the chance of light being scattered in different directions than the initial propagation distance.

The two cross-polarisation sub-matrices also differ from each other. For the 10 μm particle, the rectangular/ oval shapes in these sub-matrices are completely gone and a whole new shape arises. These new shapes even show up at low scattering angles, indicating that after travelling long enough through the particle without being scattered into high scattering angles, the polarisation component of the light will change.

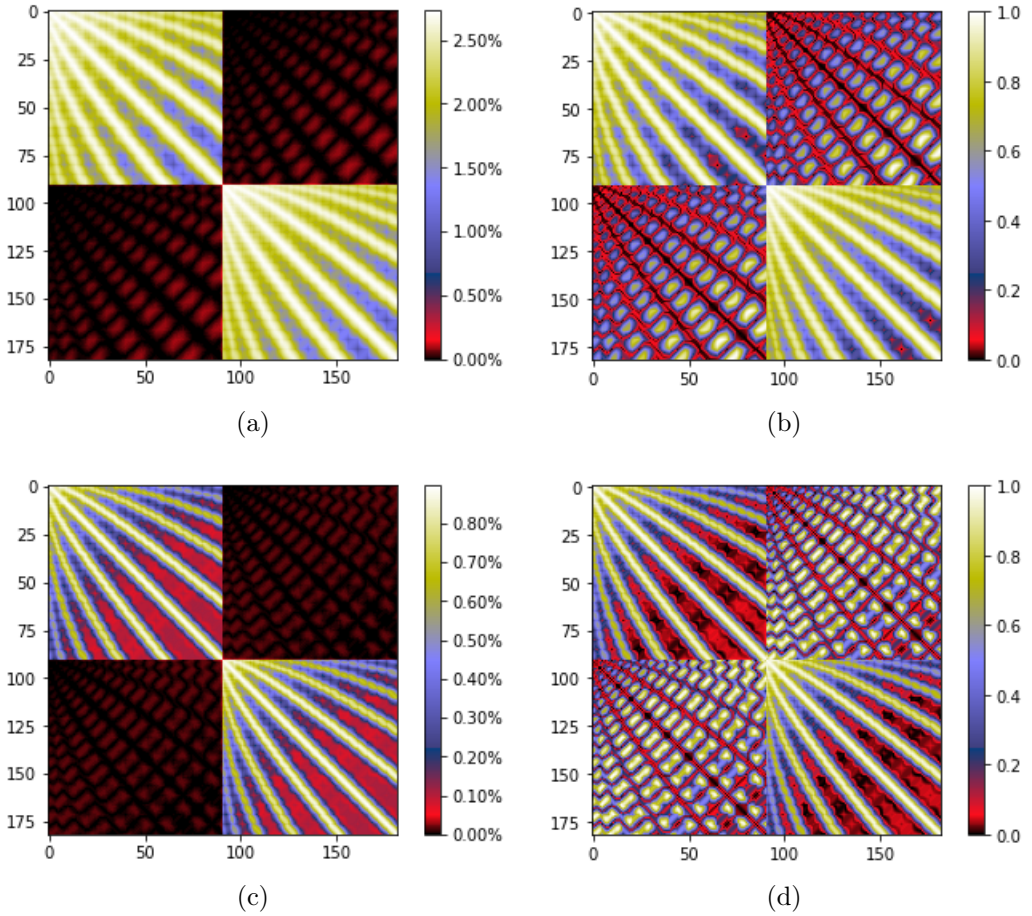

Figure 4.4: Simulated polarisation complete TM elements, measured with a hexagonal grid of 91 individual modes, of a single polystyrene sphere with diameter of (a) 5 μm and (c) 10 μm. (b) & (d): Normalised TMs of respectively (a) & (c) (each sub 91x91 matrix is normalised individually).

4.2 Experimental results

When experimentally measuring the TMs of our samples, we need to take into account that our samples are deposited on a glass cover slide. Although the glass should not scatter the light, measuring the TM of our glass gives us some insights on the fidelity of our setup alignment. If the TM of our glass shows no sign of polarisation changed scattered light, we conclude the setup is aligned properly; the two numerical aperture objectives are in focus and the glass is perpendicular to the optical axis. Besides, if the glass is not as clean as needed, some aberrations will show up in the glass TM.

An example of such an experimentally measured TM of our glass cover slide is shown in Fig. 4.5 (a). Notice the intense diagonal and much less intense side diagonals, these show the minimal overlap of neighbouring modes. Taking a closer look at the diagonal elements tells us that most of the light is indeed propagating in the forward direction through the glass and not being scattered (Fig. 4.5 (b)). Although these elements should ideally be 1.0 or close to 1.0, as shown in Fig. 2.3 (b), our experimental achieved elements around 0.8 give us a pretty nice non-scattering behaviour of the glass cover slides used in our experiments.

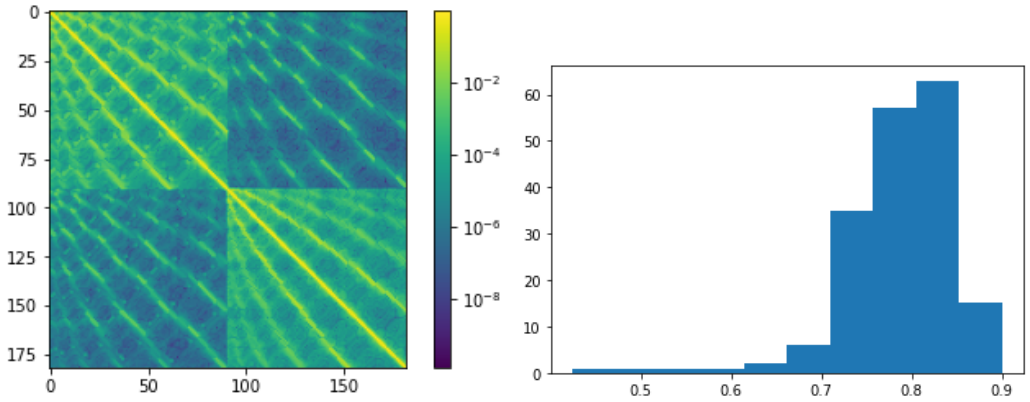

(a) (b)

Figure 4.5: (a) Polarisation complete TM of glass cover slide. (b) Histogram of diagonal elements of TM of glass cover slide.

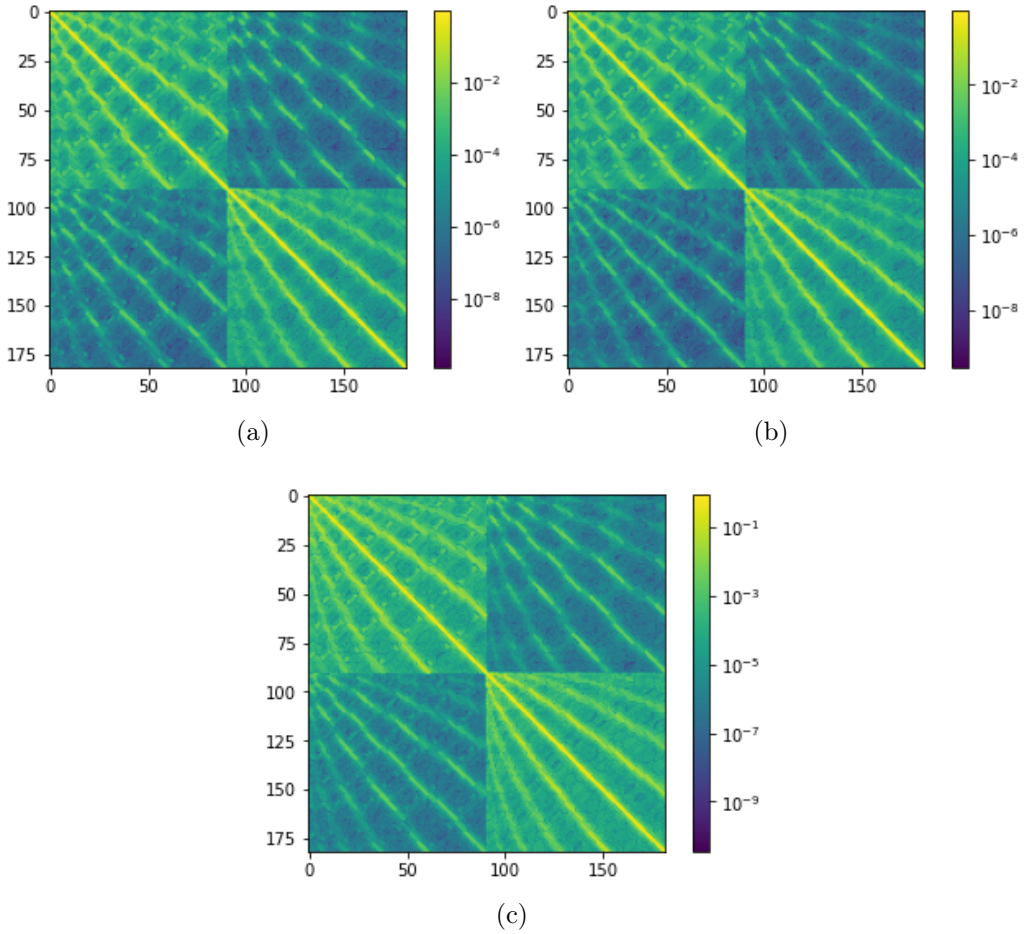

Figure 4.6: Polarisation complete TMs of single polystyrene spheres with diameters of (a) 1.58 μm, (b) 5 μm & (c) 10 μm.

Experimentally measured polarisation complete TMs for all three single polystyrene spheres with different sizes are presented in Fig. 4.6. These TMs do not look like the simulated TMs, except maybe for the intense diagonal, but rather like the glass TM. This can be explained in several different ways.

Firstly, we focus on a raw data image of the field of view containing a single polystyrene sphere with a diameter of 1.58 μm (Fig. 4.7), used during the measurement of Fig. 4.6 (a). The single particle is, compared to the field of view, really small. This means that most of the light just passes next to

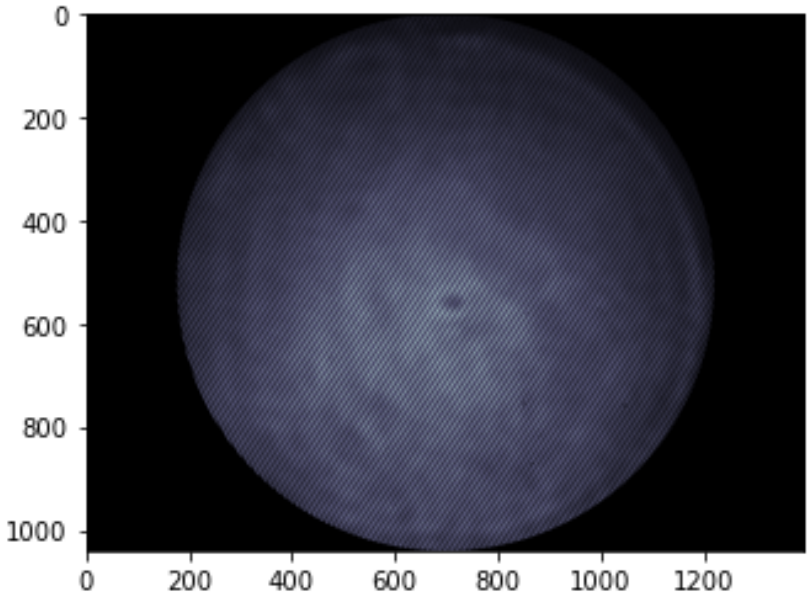

Figure 4.7: Raw data image of field of view with single polystyrene sphere with diameter of 1.58 μm.

the particle without interacting with it. Besides, the scattered modes created by the particle do not fill up the complete field of view, but rather only a small circular area in the center around the particle.

A solution to focus on these scattered modes while getting rid of the unscattered light, is by filtering in real space. By selecting a small circular area, around the center of the field of view image, all the scattered light vectors are selected while the unscattered light vectors get deleted. A Gaussian distribution is added over this area, just like the initial raw data image captured intensity is a Gaussian distribution. Unfortunately this increases noise and results in more overlap of the transmitted vectors in the detection field. Thereby broadening the side-diagonals in the measured TMs, which in turn lose the information they contained. The smaller the chosen circular area is, the bigger the noise and resulting side diagonals will appear in the TM.

Taking a different point of view and looking at both polarisation complete experimentally resolved TMs of glass and single polystyrene particles, one could say they look almost identical. This is of course not true, since we know

a single scattering sphere was present during the experimental analysis, but we can use their similar characteristics to our advantage. Two matrices A & B, with a phase shift difference, relate to each other by:

$$A \approx Be^{i\phi}, \tag{19}$$

with $\phi \approx argmin(||A - B||)$. Rewriting Eq. (19) gives:

$$\phi \approx Arg(tr(B^{+}A)), \tag{20}$$

where B^{+} is the conjugate transpose of matrix B.

By calculating the phase shift ϕ between two matrices and correcting them, one can subtract them from one another to get rid of the identical information between the two matrices. This is done for all single polystyrene experimentally measured polarisation complete TMs of Fig. 4.6. By first normalising these TMs and the measured glass TMs of the glass cover slide used on which the particle was deposited, the phase shift between the two could be determined using Eq. (20). The resulting normalised & corrected TMs are shown in Fig. 4.8.

For both the 1.58 μm & 5 μm diameter polystyrene TMs (Fig. 4.8 (a & b)), this did not bring forth any new details that relate to our single scattering particles. However, this did happen for the 10 μm polystyrene sphere, which is shown in Fig. 4.8 (c). The cross-polarisation sub-matrices show a spherical shape, in between the side diagonals. This correlates nicely with the simulated TMs in section 4.1, although the shapes are not comparable. Noticeable is the brick wall pattern present in all four sub-matrices. Where all diagonals and side-diagonals are continuous, there are alternating cross diagonals that stand out and create this brick wall pattern.

This pattern did not show up in the simulated TMs, and is something that has not been documented before. However, by taking a close look at both the TM of the glass cover slide of the 1.58 μm polystyrene experiment and the TM of the particle itself (Fig. 4.5 (a) & Fig. 4.6 (a)), these same cross diagonals might be present in the cross-polarisation sub-matrices. Normalising these matrices just makes everything dark except the central diagonal, but with some imagination the brick wall pattern is visible to some extent in the cross-polarisation sub-matrices.

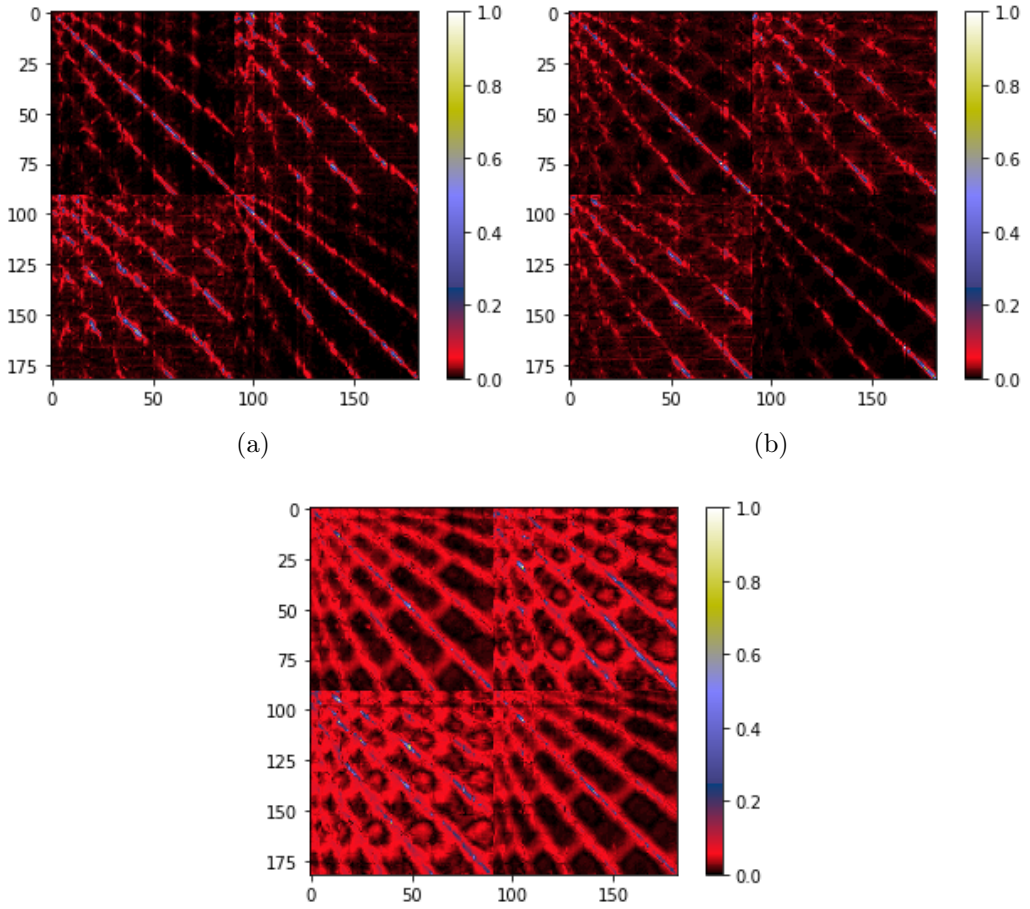

Figure 4.8: Normalised and for glass corrected TMs of single polystyrene spheres with diameters (a) 1.58 μm, (b) 5 μm & (c) 10 μm.

This is even more clear in the reflection matrices. Since the setup not only captures all the transmitted modes, but also the reflected modes, we can calculate the reflection matrix. Both the reflection matrices of the glass cover slides and single polystyrene particles (Fig. 4.9) show this brick wall pattern. The cross-polarisation sub-matrices once again get more intense when a particle is present, whereas with glass there is no polarisation shift of the light and all the sub-matrices have the same intensity.

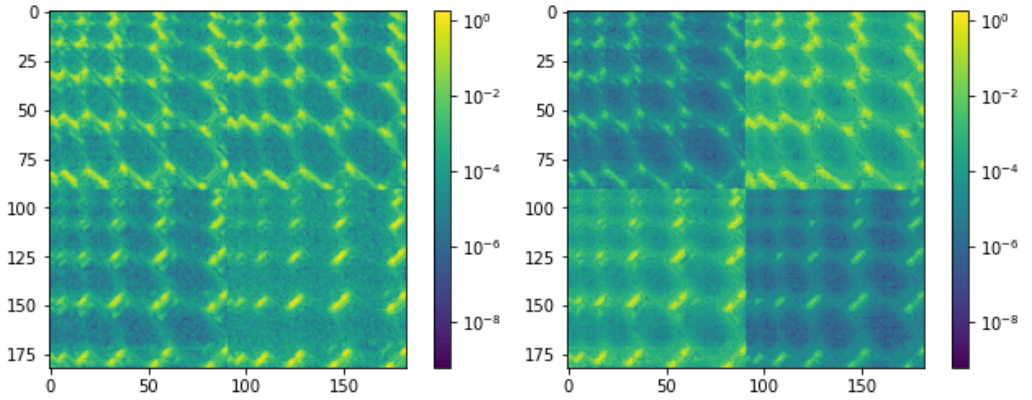

(a) (b)

Figure 4.9: Reflection matrix of (a) glass cover slide and (b) single polystyrene sphere with diameter of 1.58 μm.

4.3 Data analysis

Besides these experimentally retrieved polarisation complete TMs of single polystyrene spheres, the raw images used to calculate the matrices can give some new insights. By using both Eq. (17) and off-axis holography theory, the amplitude and phase patterns of a single field pattern can be reconstructed. By first taking the Fourier transform of an intensity pattern, such as the raw data image in Fig. 4.7, one ends up with the pattern shown in Fig. 4.10 (a). Here, the three orders do not overlap. By filtering the out the 0 and the +1 orders, and re-centering around the -1 order, the inverse Fourier transform of the signal in Fig. 4.10 (b) can give either a reconstruction of the amplitude of the field or the phase of the field.

In the resulting amplitude plot, presented in Fig. 4.10 (c), the single polystyrene sphere is visible. This is to be expected, since it was also present in the initial intensity pattern captured by the camera. The reconstruction of the phase pattern however does not have this spherical particle in the center of its plot (Fig. 4.10 (d)). This indicates that light passing through a single polystyrene sphere, of 1.58 μm in diameter, is not delayed or slowed down by scattering events. This would mean a phase shifted circular shape should be present in the center of the reconstructed phase plot, which we do not have.

Since the polystyrene spheres with a diameter of 10 μm were the only size

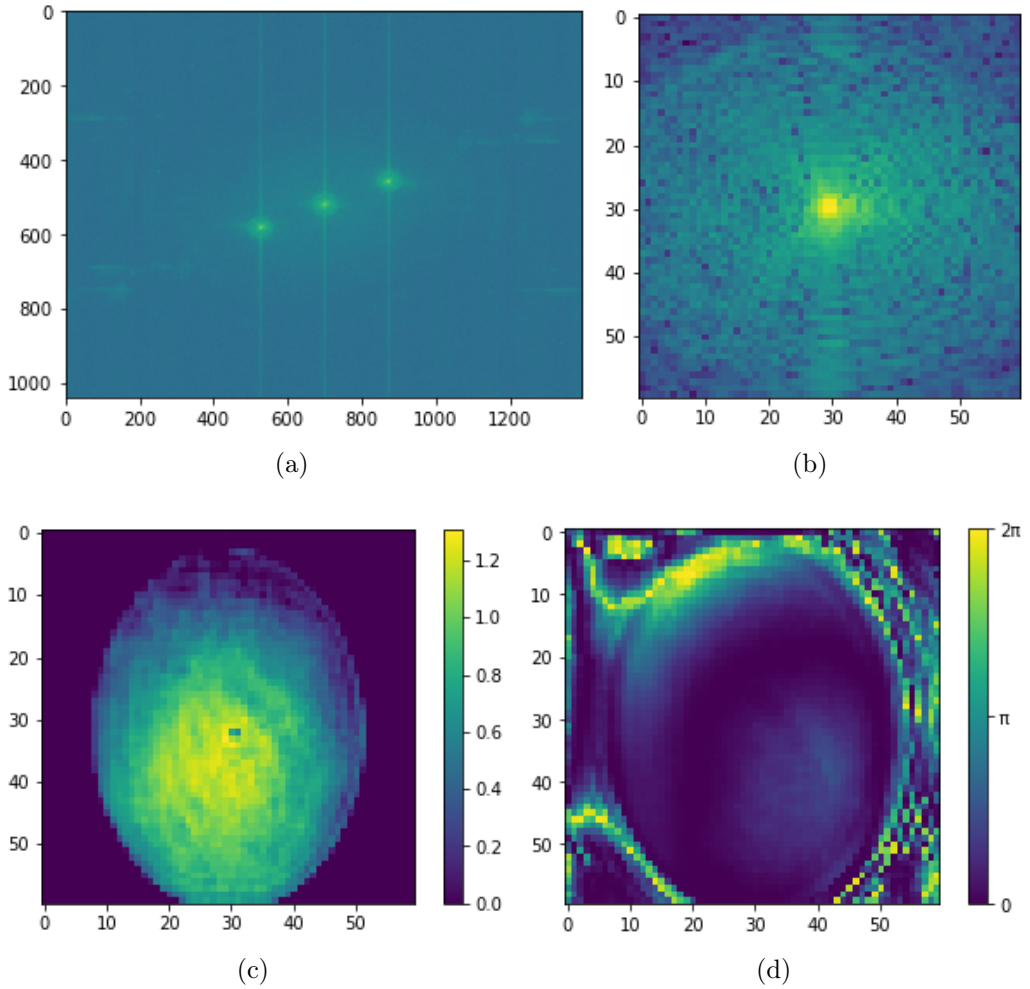

Figure 4.10: (a) Complete Fourier transform of intensity pattern of Fig. 4.7. (b) Fourier transform filtered and shifted around -1 order. Amplitude (c) & phase (d) plots of single polystyrene particle with diameter of 1.58 μm.

to show up in the experimentally measured polarisation complete TMs, we now look at their amplitude and phase plots (Fig. 4.11).

The amplitude plot clearly shows that a big single particle is present in our field of view, which blocks and scatters a lot of the light. The particle also shows up in the phase plot, where the centre of the sphere has phase shifted the transmitted light for half a wavelength. The concentric rings in

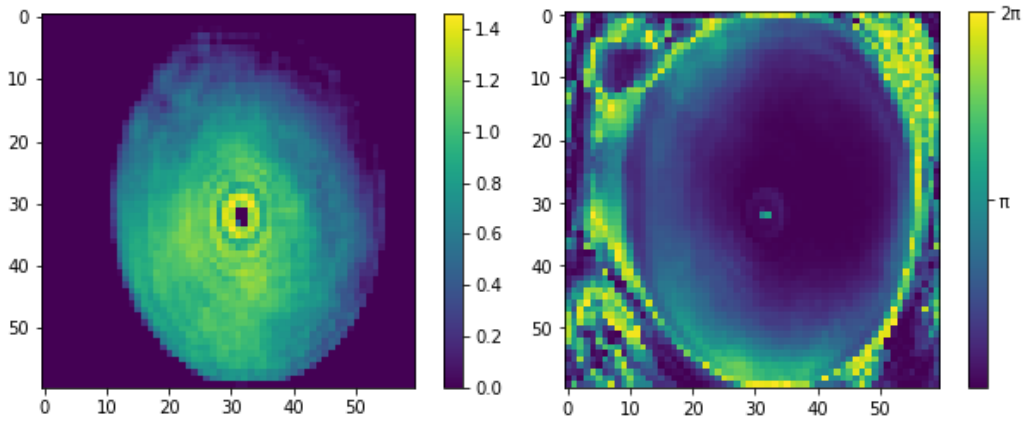

(a) (b)

Figure 4.11: (a) Amplitude & (b) phase plots of single polystyrene particle with diameter of 10 μm.

the amplitude plot indicate the particle is not perfectly in focus.

This is even clearer in the raw data image of our polystyrene sphere with a diameter of 5 μm, as visualised in Fig. 4.12 (a). The big concentric rings almost fill the complete field of view, indicating the particle is completely out of focus. Here, the picture is nothing more than a time stamp visualising the intensity of the propagating transmitted field at that time, in this case the position where the camera is placed. In the Fourier transform, the picture is transformed to the frequency domain. By multiplying the Fourier transform with a phase grid, the phases of the frequencies get changed. Thereby altering the position where the intensity field is captured.

After inversing the phase-changed Fourier transform, both the amplitude and phase plots can be retrieved, which are now representations of images taken at a different focus point. By doing this with different phase grids, and comparing the resulting amplitude and phase plots, the ideal amplitude and phase plots, which are in focus, can be reconstructed. Fig. 4.12 (b) & (d) show these optimal amplitude and phase plots, reconstructed from the initial raw data image in Fig. 4.12 (a).

In the amplitude plot, light is being blocked or scattered by one or two particles. It is not clear whether there is a single particle in our field of view, or if there are two particles packed together. However, after looking at the

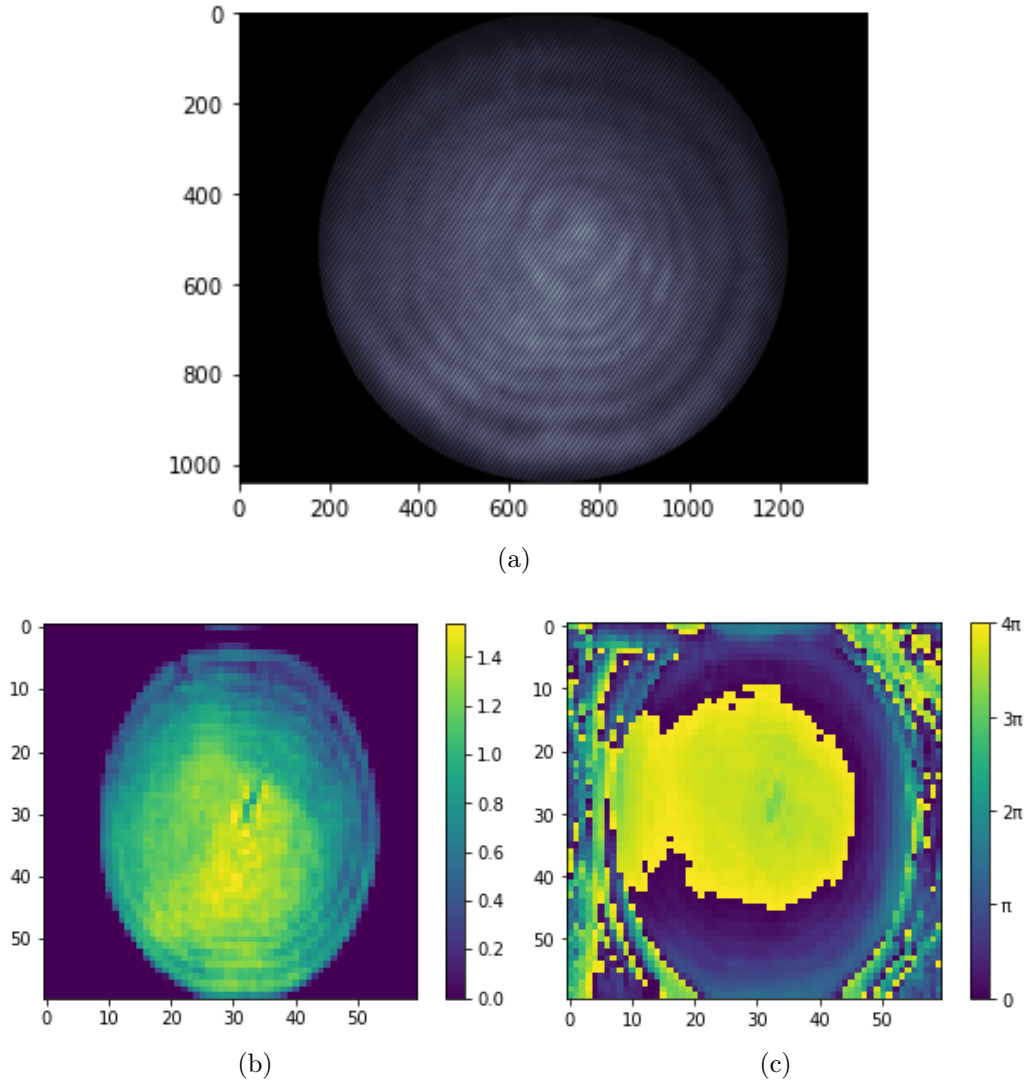

Figure 4.12: (a) Raw data image of field of view with single polystyrene sphere with diameter of 5 μm. (b) Amplitude & (c) phase plots of single polystyrene particle with diameter of 5 μm, after Fourier transform was shifted.

amplitude plot of the polystyrene particles of 1.58 μm in diameter (Fig. 4.10 (c)) and 10 μm in diameter (Fig. 4.11 (a)), we know we should be able to see one clear spherical shape that is less intense than its surroundings. Here we can distinguish two such shapes, more or less overlapping, meaning for this

measurement there were two polystyrene spheres in our field of view. In the phase plot they also show up, albeit minimally.

Discussion

As pointed out by the results of the polystyrene spheres of 5 μm in diameter, the focusing onto the surface of these spheres is not easy. In fact, the focusing procedure that has been used in this setup before, and also during this research, works better for big & flat surfaces. Even then there is an estimated accuracy of 1 μm. For all the experimental results shown in both sections 4.2 & 4.3, the setup was focused on the surface of the glass cover slide. This is because, after focusing on a clean part of the glass where no particles are present, the position of the objectives was not changed when we focused on a part of the glass where a particle was present. Since moving these objectives would result in a more out of focus pattern during the focusing procedure.

Besides the particles not being in the exact focal point, to get the absolute best results, they need to be in the exact centre of the field of view. Only in that position, all the incoming modes will hit the surface of the particles such that the scattering results can be compared to the simulation results. Since the alignment of the glass cover slide, with the deposited particles, is done by hand, placing the particles in the exact centre will never be as exact as it should be.

It should also be mentioned that the immersion oil moved over time, thereby changing the focus of both the numerical aperture objectives during experiments. This only happened after a new sample was mounted in the setup, after which a droplet of oil was placed in between the glass and the high numerical aperture objective (NA = 1.4). For a few days, sometimes maybe a week, the focus points changed every day slightly due to the oil movement (~ 1 μm/ day). Until eventually the oil reached its final steady state and stayed constant.

Besides these minor issues and difficulties, the results are looking promising. Especially for the biggest polystyrene particle that we analysed (10 μm in diameter), the TM is comparable to the simulated TM. The shapes in the cross-polarisation sub-matrices are not exactly identical, but they do show up in the same areas. The brick-wall pattern is probably due to some minor overlap between neighbouring modes in the detection fields that we cannot cancel out completely. They show up in both the experimentally measured

TMs of our single polystyrene particles and our glass cover slides. Besides, they are particularly obvious in the reflection matrices of both the glass cover slide and the single polystyrene particles.

For future research into transmission of small spherical particles, a better way of focusing onto these particles is needed. The out of focus 5 μm in diameter polystyrene double particles did not show up in our experimental measured TM, but later we proved that they were indeed detected by the setup. A new way of focusing this experimental setup would thus most probably visualise the 5 μm sized polystyrene particles, and maybe even the 1.58 μm diameter spheres. But for this, the estimated error of the setup should also be decreased, because an estimated error of 1 μm is too big for particles that small.

Conclusion

All in all, the TMs of single polystyrene particles with a diameter of 10 μm were successfully measured during this research. Although the smaller particles at first did not show up in our matrices, after some analysis, the scattering behaviour of these particles was indeed observed in the phase and amplitude plots of these particles. With a better focusing procedure, it will be possible to analyse particles as small as 5 μm in diameter in the future. However, for particles of 1.58 μm in diameter, or even $\sim$ 170 nm such as the 3D icosahedral quasicrystals, even more analysis steps or a different experimental setup are needed.

Bibliography

[1] J. Weiner and P.-T. Ho, *Light—matter interaction: fundamentals and applications* (John Wiley & Sons, 2003).

[2] E. V. Appleton, "Departure of long-wave solar radiation from black-body intensity", Nature **156**, 534–535 (1945).

[3] O. Virtanen, E. Constantinidou, and E. Tyystjärvi, "Chlorophyll does not reflect green light – how to correct a misconception", J. Biol. Educ. **56**, 1–8 (2020).

[4] M.-S. Kao and C.-F. Chang, *Understanding electromagnetic waves* (Springer, 2020).

[5] M. M. Malaiyandi, H. Sadar, P. Lee, and R. O'Grady, "Removal of organics in water using hydrogen peroxide in presence of ultraviolet light", Water Research **14**, 1131–1135 (1980).

[6] C. Roychoudhuri, A. F. Kracklauer, and K. Creath, *The nature of light: what is a photon?* (CRC Press, 2017).

[7] Y. Akahane, T. Asano, B.-S. Song, and S. Noda, "High-q photonic nanocavity in a two-dimensional photonic crystal", Nature **425**, 944–947 (2003).

[8] C. López, "Materials aspects of photonic crystals", Adv. Mater. **15**, 1679–1704 (2003).

[9] M. Notomi, "Theory of light propagation in strongly modulated photonic crystals: refractionlike behavior in the vicinity of the photonic band gap", Phys. Rev. B **62**, 10696–10705 (2000).

[10] A.-P. Hynninen, J. H. J. Thijssen, E. C. M. Vermolen, M. Dijkstra, and A. van Blaaderen, "Self-assembly route for photonic crystals with a bandgap in the visible region", Nature Materials **6**, 202–205 (2007).

[11] D. Shechtman, I. Blech, D. Gratias, and J. W. Cahn, "Metallic phase with long-range orientational order and no translational symmetry", Phys. Rev. Lett. **53**, 1951–1953 (1984).

[12] J. Bamberg, G. Cairns, and D. Kilminster, "The crystallographic restriction, permutations, and goldbach's conjecture", **110**, 202–209 (2003).

[13] V. Elser, "Indexing problems in quasicrystal diffraction", Phys. Rev. B **32**, 4892–4898 (1985).

[14] A. I. Goldman and M. Widom, "Quasicrystal structure and properties", Annu. Rev. Phys. Chem. **42**, 685–729 (1991).

[15] A. P. Tsai, J. Q. Guo, E. Abe, H. Takakura, and T. J. Sato, "A stable binary quasicrystal", Nature **408**, 537–538 (2000).

[16] D. Wang, T. Dasgupta, E. B. van der Wee, D. Zanaga, T. Altantzis, Y. Wu, G. M. Coli, C. B. Murray, S. Bals, M. Dijkstra, and A. van Blaaderen, "Binary icosahedral clusters of hard spheres in spherical confinement", Nature Physics **17**, 128–134 (2020).

[17] P. Pai, J. Bosch, M. Kühmayer, S. Rotter, and A. P. Mosk, "Scattering invariant modes of light in complex media", Nature Photonics **15**, 431–434 (2021).

[18] A. T. Young, "Rayleigh scattering", Applied optics **20**, 533–535 (1981).

[19] H. C. van de Hulst, *Scattering by small particles* (Dover Publications, 1981).

[20] C. F. Bohren and D. R. Huffman, *Absorption and scattering of light by small particles* (John Wiley & Sons, 1998).

[21] D. Akbulut, "Measurements of strong correlations in the transport of light through strongly scattering materials" (University of Twente, 2013).

[22] M. C. W. van Rossum and T. M. Nieuwenhuizen, "Multiple scattering of classical waves: microscopy, mesoscopy, and diffusion", Rev. Mod. Phys. **71**, 313–371 (1999).

[23] I. M. Vellekoop, "Controlling the propagation of light in disordered scattering media" (University of Twente, 2008).

[24] S. M. Popoff, G. Lerosey, R. Carminati, M. Fink, A. C. Boccara, and S. Gigan, "Measuring the transmission matrix in optics: an approach to the study and control of light propagation in disordered media", Phys. Rev. Lett. **104**, 1–4 (2010).

[25] E. G. van Putten and A. P. Mosk, "The information age in optics: measuring the transmission matrix", Physics **3** (2010).

[26] P. Pai, "Accurate statistics from optical transmission matrix measurements" (Utrecht University, 2020).

[27] P. O. Bayguinov, D. M. Oakley, C.-C. Shih, D. J. Geanon, M. S. Joens, and J. A. Fitzpatrick, "Modern laser scanning confocal microscopy", Current protocols in cytometry **85**, 1–17 (2018).

[28] G. B. de Boer, C. de Weerd, D. Thoenes, and H. W. Goossens, "Laser diffraction spectrometry: fraunhofer diffraction versus mie scattering", Particle & Particle Systems Characterization **4**, 14–19 (1987).

[29] J. F. Ramsay, "Rayleigh distance as a normalizing range for beam power transmission", in G-mtt symposium digest, Vol. 65 (IEEE, 1965), pp. 27–32.

[30] E. W. Weisstein, "Bessel function of the first kind", (2002), `https://mathworld.wolfram.com/BesselFunctionoftheFirstKind.html`.

[31] O. Dorokhov, "On the coexistence of localized and extended electronic states in the metallic phase", Solid state communications **51**, 381–384 (1984).

[32] P. Pai, J. Bosch, and A. P. Mosk, "Optical transmission matrix measurement sampled on a dense hexagonal lattice", OSA Continuum **3**, 637–648 (2020).

[33] V. A. Marchenko and L. A. Pastur, "Distribution of eigenvalues for some sets of random matrices", Matematicheskii Sbornik **114**, 507–536 (1967).

[34] J. Bosch, "Measurements of channels and time delay of light in strongly scattering media" (Utrecht University, 2020).

[35] M. Peet, "Non-commutative statistics on optical transmission matrices" (Utrecht University, 2022).

[36] M. P. di Mauro, "Helioseismology: a fantastic tool to probe the interior of the sun", LNP (2012).

[37] G. Mie, "Beiträge zur optik trüber medien, speziell kolloidaler metallösungen", Annalen der physik **330**, 377–445 (1908).

[38] N. Sultanova, S. Kasarova, and I. Nikolov, "Dispersion properties of optical polymers", Acta Phys. Pol. A **116**, 585–587 (2009).

[39] B. J. Sumlin, W. R. Heinson, and R. K. Chakrabarty, "Retrieving the aerosol complex refractive index using pymiescatt: a mie computational package with visualization capabilities", JQRST **205**, 127–134 (2018).

[40] M. Takeda, H. Ina, and S. Kobayashi, "Fourier-transform method of fringe-pattern analysis for computer-based topography and interferometry", JosA **72**, 156–160 (1982).